Precision Crystal Alignment for High-Resolution Electron Microscope Imaging

G.J. Wood and M.J. Beeching

School of Physics, University of Melbourne, Parkville, Victoria 3052, Australia.

Abstract

One of the more difficult tasks involved in obtaining quality high- resolution electron micrographs is the precise alignment of a specimen into the required zone. The current accepted procedure, which involves changing to diffraction mode and searching for a symmetric point diffraction pattern, is insensitive to small amounts of misalignment and at best qualitative. On-line analysis of the fourier space representation of the image, both for determining and correcting crystal tilt, is investigated.

1 Introduction

The standard method of crystal alignment in transmission electron microscopy involves changing to diffraction mode and searching for a symmetric selected-area point diffraction pattern [1]. The assessment of symmetry is qualitative and insensitive to small amounts of misalignment. Given a suitable specimen, diffraction from a sufficiently large area of that specimen and a patient operator, an optimistic estimate of the alignment achievable is half the operative Bragg angle (around 2mrad at 400kV). In thick, extended and relatively defect-free crystals, Kikuchi lines, rather than intensities of the diffracted beams alone, can be used to ensure an accuracy of alignment of around one tenth of the operative Bragg angle [2]. Computer simulations [3], have shown [4], that such an accuracy, while being near to the limits of present-day goniometers [5] is, barely sufficient for thicker crystals. However, to achieve this accuracy a large selected-area is required hence, the alignment is an average alignment over an extended region. In the presence of defects such as grain boundaries, individual dislocations or inclusions, there may be substantial lattice strain and localised changes in crystal orientation. Moreover, for thin crystals, a low structural rigidity and the presence of surface oxides or contaminants can result in considerable foil bending [6]. It is precisely in the crystalline regions of greatest interest and relevance to high-resolution imaging that the selected- area diffraction pattern no longer provides a sufficiently reliable indication of the local crystal orientation.

Microdiffraction and convergent beam diffraction patterns are very sensitive to crystal tilt and can be collected from very localised crystalline regions. However, the accurate crystal alignment in these diffraction modes does not necessarily translate to accurate alignment for an image. The changes in objective and/or condenser lens excitations which are required upon returning to the conventional high-resolution imaging mode are almost certain to alter the angle of

inclination of the incident beam at the specimen, changing the crystal alignment.

This report investigates the determination and correction of crystal tilt based on detail observed in the image. Optical diffractograms contain the amplitude component of the fourier space representation of an image and are used widely as an image diagnostic tool. It has been shown [4], that diffractograms are insensitive to small amounts of misalignment. Our investigation examines both the amplitude and the phase of the fourier space representation of the image hence, has the potential to explore all image information, including contrast displacements in the image.

2 Method and hardware

2.1 Method

Consider an image $f(x,y)$ and its fourier transform $\mathcal{F}(u,v)$ given by:

$$\mathcal{F}(u,v) = \int\int f(x,y)e^{2\pi i(ux+vy)}dx\,dy \tag{1}$$

or in its discrete form

$$\mathcal{F}(u,v) = \sum_x \sum_y f(x,y)e^{2\pi i\left(\frac{ux}{N}+\frac{vy}{M}\right)} \tag{2}$$

where the image is sampled with N by M pixels.

The symmetry of the image is averaged over all unit cells in the field of view and represented in the transform $\mathcal{F}(u,v)$ with an improved signal- to-noise ratio. High symmetry crystal orientations are sought by examining amplitude and phase relationships for a range of crystal tilts. The aligned crystal transform symmetry will be structure and projection dependent hence, to be completely general, a range of symmetry searching algorithms need to be considered. In projection, a high percentage of structures found in nature have inversion symmetry. For this

initial investigation, we develop the technique around the search for an inversion centre.

$\mathcal{F}(u,v)$ can be split into its real and imaginary parts as follows

$$\begin{aligned} Re(u,v) &= Real[\mathcal{F}(u,v)] \\ &= \sum_x \sum_y f(x,y) \cos 2\pi \left(\frac{ux}{N} + \frac{vy}{M}\right) \end{aligned} \tag{3}$$

$$\begin{aligned} Im(u,v) &= Imag[\mathcal{F}(u,v)] \\ &= \sum_x \sum_y f(x,y) \sin 2\pi \left(\frac{ux}{N} + \frac{vy}{M}\right) \end{aligned} \tag{4}$$

For an inversion centre in real space, the imaginary part of $\mathcal{F}(u,v) = Im(u,v)$ will be identically zero.

Now the introduction of any asymmetry into the image, as results from crystal tilt, will cause $Im(u,v)$ to have non-zero values. Therefore the basic method is to minimise the quantity $\mathcal{IR}$, given by

$$\mathcal{IR} = \sum_{u,v} (|Im(u,v)|) / \sum_{u,v} 1 \tag{5}$$

by adjusting crystal tilt, with the minimum value of $\mathcal{IR}$ hopefully corresponding to zero crystal tilt.

2.2 Hardware

Crystal tilted images were simulated on computer using the Melbourne University Multislice (MUM) program suite [7] and these images were then fourier transformed and analysed using the SEMPER program package [8].

For high-speed on-line analysis of real images at the microscope, specialised hardware consisting of:

1. Mercury MC3200 parallel processor

2. A collection of DataCube video rate processing elements comprising:

- 1 DIGIMAX acquisition and display module
- 3 ROISTORE digital video data banks
- 2 MAX–SP complex arithmetic logic units
- 1 FEATUREMAX video rate histogram module

has been configured as shown in fig. 1. Under the control of the SUN workstation, the DataCube boards acquire and display data at video rate and the parallel processor performs the fourier transformations.

3 Application to ideal images

3.1 Specimen details

Investigations were made using computer simulated images of TiO_2 in the [001] orientation, for thicknesses between 33 and 222 Å for the defocus values -400, -800 and -1200 Åat 400 kV. A tilt series for each of these conditions was then computed over the tilt range, zero to the first Bragg reflection (3.6 mrad). For each of these images the fourier transform was taken then, $\mathcal{IR}$ described by equation (5) calculated. $\mathcal{IR}$ values are displayed as intensity, as a function of the 2 possible dimensions of crystal misalignment, in tilt maps, as shown in fig. 2. The aligned crystal $\mathcal{IR}$ value is located at the centre of the plot. Figs. 2-16 compare tilt maps ($\mathcal{IR}$ variations with crystal tilt) for a range of specimen thicknesses, defocii, plot depths and plot widths as labelled.

3.2 Discussion

All of the plots show a smooth well structure which is promising since a ragged well structure would complicate practical location of the minimum. In practice a minimum is not of much use if you need to scan over a large range of tilts to

find it. The wells are deeper for the thicker specimens as is expected due to the increased effect of tilt at larger thicknesses. Note also the change in the wells for different defocii. This could be very useful since defocus is an easily changed parameter and could be set to give the best results for finding the well minimum.

4 Problems in real images

4.1 Origin centre

The biggest problem associated with real images is locating a suitable origin for the fourier transform. Consider an image $f(x,y)$ being shifted (relative to its inversion centre) by an amount (α,β). The fourier transform then becomes

$$\begin{aligned}\mathcal{F}'(u,v) &= \int\int f(x-\alpha,y-\beta)e^{2\pi i(ux+vy)}dxdy \\ &= e^{2\pi i(u\alpha+v\beta)}\int\int f(x,y)e^{2\pi i(ux+vy)}dxdy \\ &= e^{2\pi i(u\alpha+v\beta)}\mathcal{F}(u,v) \end{aligned} \tag{6}$$

Thus a phase shift is introduced, and the imaginary part becomes (using discrete rotation)

$$Im'(u,v) = \sin 2\pi\left(\frac{u\alpha}{N}+\frac{v\beta}{M}\right)Re(u,v) \tag{7}$$

(once again using the inversion symmetry of $f(x,y)$) Similarly the real part becomes

$$Re'(u,v) = \cos 2\pi\left(\frac{u\alpha}{N}+\frac{v\beta}{M}\right)Re(u,v) \tag{8}$$

We can see therefore that even a small change in the origin can have a dramatic effect on the result. For example a 1 pixel shift will cause the value of $Im'(u,v)$ to equal $Re(u,v)$ at a point halfway to the edge of the unit cell. Before discussing ways of correcting for this shift, it should be noted that the majority of beams away from the "central region" have very small magnitude, therefore we only

need to average over the "central region". In particular, if we only average over a region where the *sine* function in equation (7) is sufficiently close to 0 then the effect of the origin shift should not be as great. This limited averaging should also be helpful when images containing noise are considered. (See section 4.3) To show the effect of this limited averaging on images with no origin shift, the analysis corresponding to fig 4 was repeated with the averaging only being performed on the region shown in fig 17. The resultant well with the same parameters is shown in fig 18. We see that not only has the well structure been retained (as expected) but it has been improved by considering only the beams with any significant magnitude.

Now for the correcting of the origin shift. In the case where the image has an inversion centre (i.e. no tilt) the equations for $Im'(u,v)$ and $Re'(u,v)$ hold, and they can be inverted for specific values of u and v to determine α and β. For example, along the line $(u,0)$ we have

$$\alpha = \frac{N}{2\pi u}\tan^{-1}\left(\frac{Im'(u,0)}{Re'(u,0)}\right) \tag{9}$$

and along the line $(0,v)$ we have

$$\beta = \frac{M}{2\pi v}\tan^{-1}\left(\frac{Im'(0,v)}{Re'(0,v)}\right) \tag{10}$$

Other equations can be derived, and all can be used to easily calculate α and β as shown in figs 19 - 20. (Note that if the value of $Im'(u,v)$ or $Re'(u,v)$ is "too small" the value obtained will be far from accurate.)

As stated previously, these equations work fine if the image has an inversion centre, however in the case where some asymmetry is present the equations for $Im'(u,v)$ and $Re'(u,v)$ become

$$\begin{aligned} Im''(u,v) &= \sin 2\pi\left(\frac{u\alpha}{N}+\frac{v\beta}{M}\right)(Re(u,v)+Real[\mathcal{F}(\delta)]) \\ &\quad +\cos 2\pi\left(\frac{u\alpha}{N}+\frac{v\beta}{M}\right)Imag[\mathcal{F}(\delta)] \end{aligned} \tag{11}$$

$$Re''(u,v) = \cos 2\pi\left(\frac{u\alpha}{N}+\frac{v\beta}{M}\right)(Re(u,v)+Real[\mathcal{F}(\delta)]) - \sin 2\pi\left(\frac{u\alpha}{N}+\frac{v\beta}{M}\right) Imag[\mathcal{F}(\delta)] \quad (12)$$

where the image is now given by the sum of a component with inversion symmetry, and a deviation $\delta(x,y)$ caused by some asymmetry. Clearly these equations do not have a simple solution for α and β and so an alternate method needs to be used.

One such method that could be used is to calculate for each point, a number indicating the amount of inversion symmetry about that point. That is, calculate the sum of difference squared of the pixels around the chosen point. The point that gives a minimum value can be selected as the origin.

This method only needs to be applied to a quarter of the points in a single unit cell (or refined cell) since a shift of half a unit cell only introduces a sign factor which does not affect any of the quantities calculated here. Reduction is strictly only valid for a lattice of identical cells however, we have found that some variation can be tolerated. Moreover, this method has the advantage that once the origin has been found and the fourier transform performed, all of the desired quantities can be calculated immediately; whereas, if the origin is determined after the fourier transform is performed then a phase shift needs to be calculated for each of the points that will be involved in subsequent calculations, and is thus far more time consuming than determining the origin by the least squared method.

To test this method a program for calculating the "best" origin was written and used to determine the origins for a number of images that were used in section 2. The same analysis was then performed on these images and the results are shown in figs 21 - 26. Note that now the wells are shallow and this is likely to happen in practice with experimental images of unknown origin.

If this procedure is to be used in the on-line set-up described earlier, using the parallel processor, the time taken would typically be a fraction of a second and would therefore permit real-time interactive correction of tilt at the microscope.

The method of course needs to be able to find or be told the position of a single cell. From a calculating point of view, a unit cell could be calculated (and refined if required) using previously considered techniques [7], however it is hoped that current work into drift correction will enable the user to mark out a single cell (and region of interest) using a mouse type arrangement prior to any additional calculations.

4.2 Edge effects

"Edge effects" arise in a number of situations, but they can all be attributed to the fact that the image can be in any orientation, with any unit cell type and of any magnification (within limits), whereas high-speed fourier transform algorithms require a square array of specific size. For example, if we have non-orthogonal cells, rotated cells or a non-integral number of cells in the image, the results will deviate from those in the ideal case.

As an example of these effects the same images as used in section 1, but now with the addition of some extra pixels around the edge of the images, were fourier transformed and the corresponding tilt maps produced. The results and details are shown in figs 27 – 32. Here we see the unpredictable nature of edge effects. In figs 27 – 29 a well structure has been retained but it has been deformed while in figs 30 – 32 the well structure eventually disappears and is replaced by a completely useless structure as far as tilt detection is concerned. It is important to note in both cases that a small amount of edge pixels did not completely destroy the well structure, this coupled with the fact that that these tilt maps were produced with only one cell and that in practice there will be many cells, (thereby reducing edge effects considerably,) leads to the conclusion that edge

effects should not have an effect as large as that shown in these figures. The combined contribution from the different types of edge effects could however, make a significant change to the tilt maps.

A region, once found, could be transformed to the desired square array by a linear transformation, however this would be both time consuming, or would most probably involve some loss of data (see for example fig 33). Note that any refined cell could be transformed to a square array, and this could be a possible avenue to follow in the future.

An alternative approach is to mask off the unwanted region with a blank (or constant) area, thereby causing the fourier transform to simply be an oversampled version of the ideal fourier transform, plus some small deviations due to the finite sampling of the image. (eg. Pixels not falling exactly on cell boundaries etc.) To test the effectiveness of masking, the same calculations used to produce figs 27 – 32 were repeated with the extra edge pixels (fractional unit cells) blanked out. The results and details are shown in figs 34 – 39. This technique appears to work very nicely with the well structures being retained in all cases.

4.3 Noise

Noise of course is present in all real images and to determine it's effect some ideal images (yes as used in section 1) had noise added in SEMPER using the verb NOISE with an appropriate dose. Limited averaging of the beams, as discussed in section 4.1, was also performed to determine its usefulness. Details and results are shown in figs 40 – 41. Notice that due to the averaging nature of the analysis noise has little effect on disturbing the well structure.

4.4 Other asymmetries

The success of this method in detecting crystal tilt depends on the presence of the tilt alone as the asymmetry factor in the images. Other asymmetries will

therefore limit the accuracy of this method. As an example, an image with beam tilt present was used and the results are shown in fig 42. Notice that the "well" has lost its smooth structure and therefore this and other types of asymmetries (eg. astigmatism) will have to be minimised in order to fully exploit this method.

5 Conclusion

Though the method shown here is successful on ideal images, its effectiveness on real images can be expected to be lessened, the extent of this lessening is not completely clear and will have to be assessed once images from the electron microscope are used. However, it seems clear that the success of this method will rely greatly on the ability to have stable images coupled with an interactive environment. Automated drift correction would almost certainly help the microscope operator monitor and collect images from the same region of specimen as crystal tilt is varied.

6 References

[1] D.K. Philp and L.A. Bursill, J. of Solid State Chem. 10 (1974), 357-370.

[2] S. Kikuchi, Proc. Imp. Acad. Japan 4 (1928) 271.

[3] L.A. Bursill and G.J. Wood, Phil. Mag. A38 (1978) 673-689.

[4] D.J. Smith, W.O. Saxton, M.A. O'Keefe, G.J. Wood and W.M. Stobbs, Ultamicroscopy 11 (1983) 263-282.

[5] L.A. Bursill, A.E.C. Spargo, D. Wentworth and G.J. Wood, J. Appl. Cryst. 12 (1979) 279-286.

[6] D.J. Smith, L.A. Bursill and G.J. Wood, Ultramicroscopy 16 (1985) 19-32.

[7] M.J. Beeching, Univ. of Melbourne, 4th year report (1988).

[8] W.O. Saxton, T.J. Pitt and M. Horner, Ultramicroscopy 4 (1979), 343.

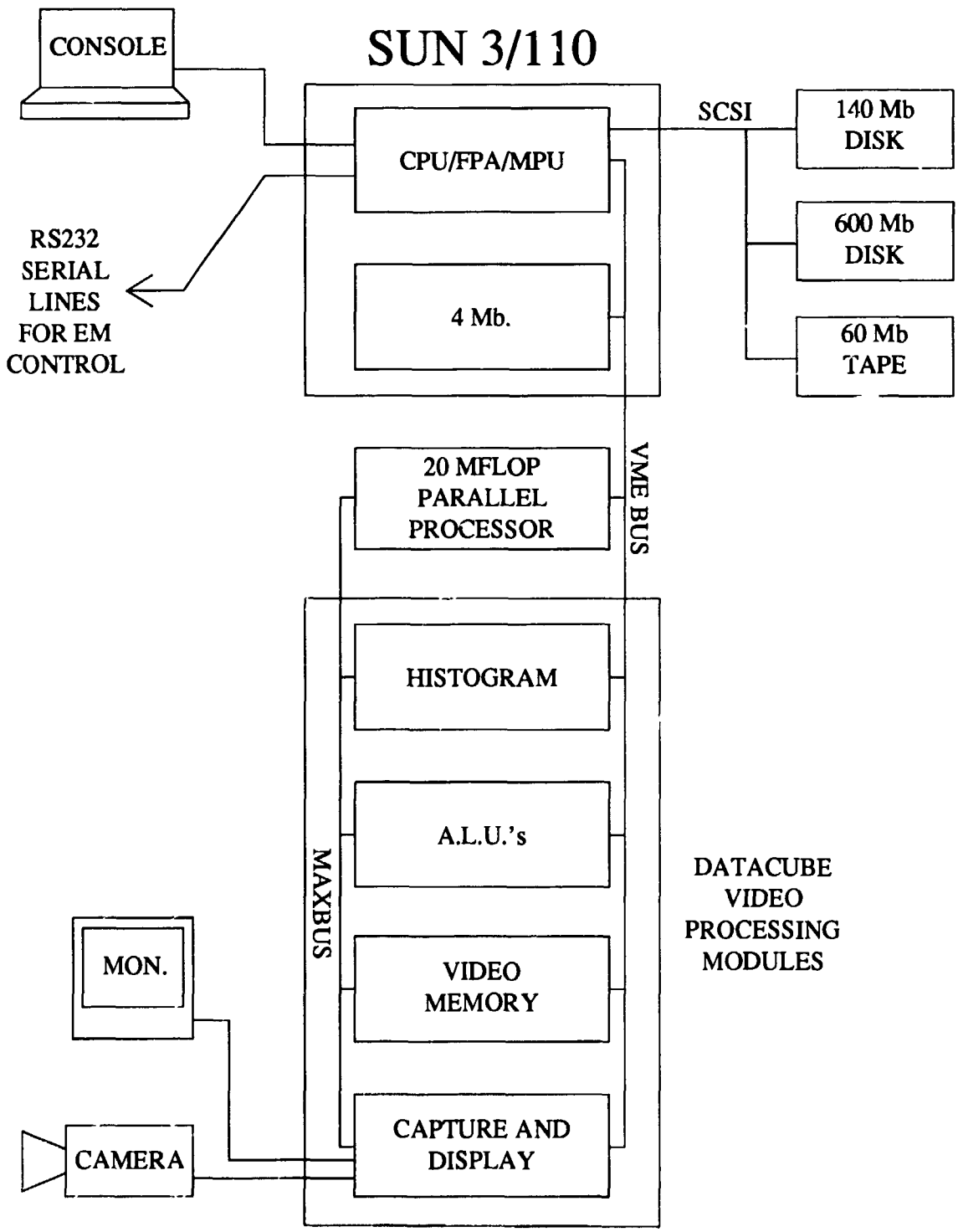

Figure 1: Hardware setup.

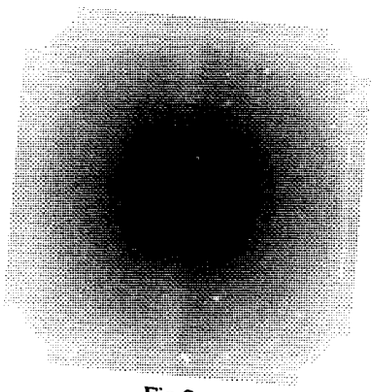

Fig 2
Def = -400 Å
Th = 44 Å
Depth = 169.4
FWHM = 3.40 mrad

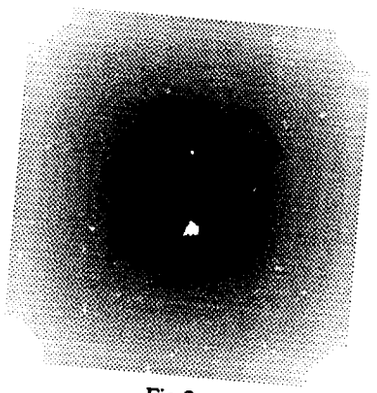

Fig 3
Def = -800 Å
Th = 44 Å
Depth = 89.1
FWHM = 3.89 mrad

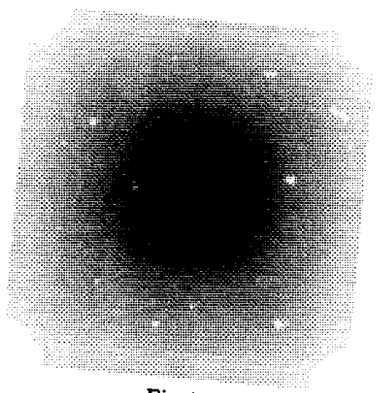

Fig 4
Def = -1200 Å
Th = 44 Å
Depth = 164.6
FWHM = 3.49 mrad

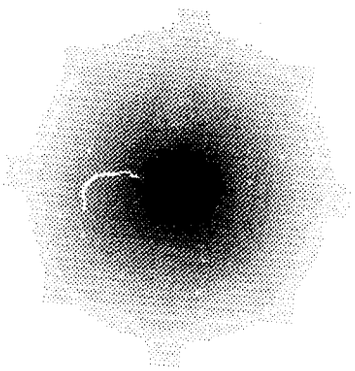

Fig 5
Def = -400 Å
Th = 88 Å
Depth = 363.2
FWHM = 2.05 mrad

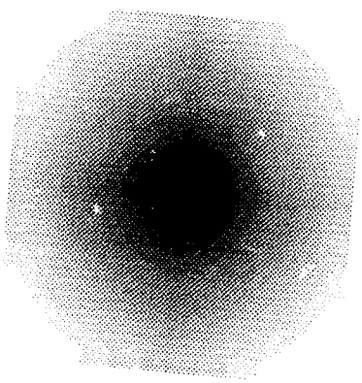

Fig 6
Def = -800 Å
Th = 88 Å
Depth = 349.1
FWHM = 2.72 mrad

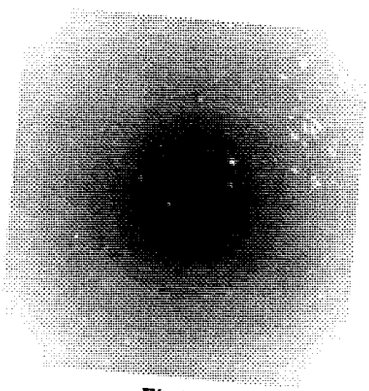

Fig 7
Def = -1200 Å
Th = 88 Å
Depth = 363.4
FWHM = 3.46 mrad

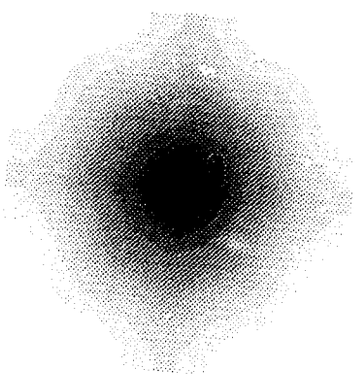

Fig 8
Def = -400 Å
Th = 133 Å
Depth = 536.2
FWHM = 2.12 mrad

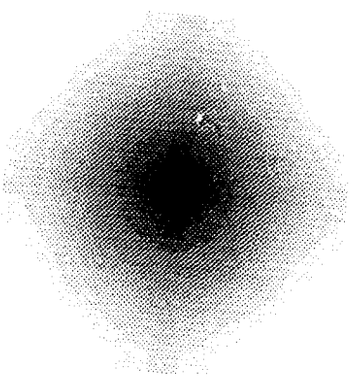

Fig 9
Def = -800 Å
Th = 133 Å
Depth = 511.2
FWHM = 1.92 mrad

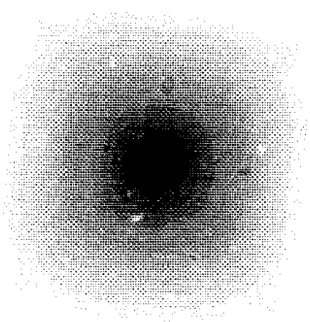

Fig 10
Def = -1200 Å
Th = 133 Å
Depth = 484.6
FWHM = 1.94 mrad

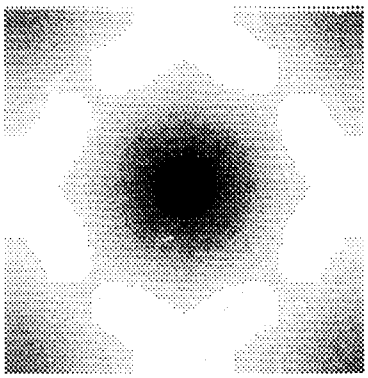

Fig 11
Def = -400 Å
Th = 177 Å
Depth = 669.4
FWHM = 1.34 mrad

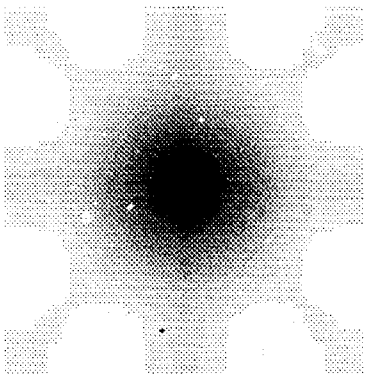

Fig 12
Def = -800 Å
Th = 177 Å
Depth = 623.3
FWHM = 1.52 mrad

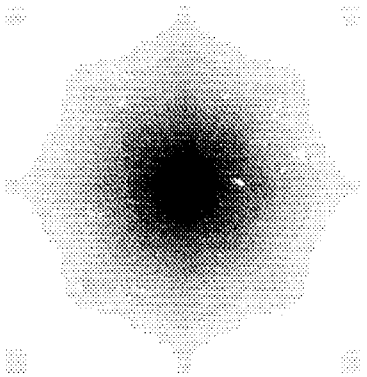

Fig 13
Def = -1200 Å
Th = 177 Å
Depth = 612.1
FWHM = 1.41 mrad

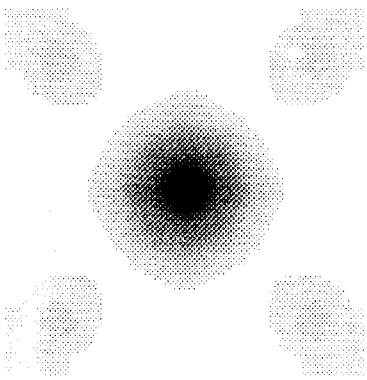

Fig 14
Def = -400 Å
Th = 221 Å
Depth = 620.0
FWHM = 1.22 mrad

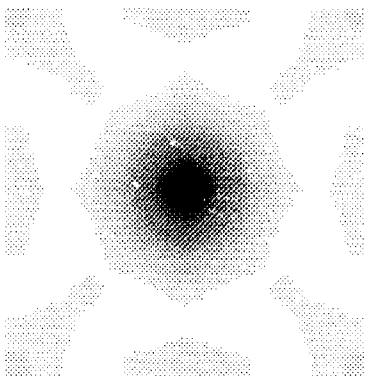

Fig 15
Def = -800 Å
Th = 221 Å
Depth = 528.5
FWHM = 1.23 mrad

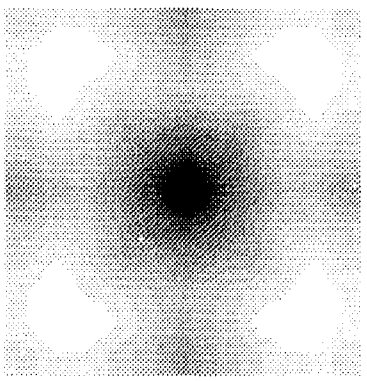

Fig 16
Def = -1200 Å
Th = 221 Å
Depth = 622.4
FWHM = 1.31 mrad

Fig 17

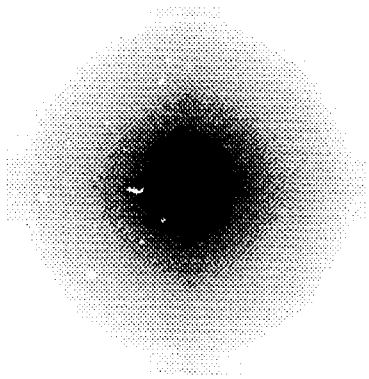

Fig 18
cf. Fig 6
Def = -800 Å
Th = 88 Å
Depth = 3729.4
FWHM = 3.83 mrad

Limited averaging

Fig 17: The modulus of a typical power spectrum obtained during the calculation of the tilt map shown in Fig 6. Here the very faint beams have been deliberately boosted to become visible out to the approximate range that was chosen for the averaging of the imaginary part.

Fig 18: Tilt map resulting from the limited range of averaging shown in Fig 17.

Real part.

0.462	-0.017	-0.327	-0.006	-0.281	0.014	0.295
-0.017	0.523	0.286	0.696	-0.274	0.433	0.014
-0.343	0.291	-0.571	0.004	-0.552	-0.279	-0.297
-0.006	0.713	0.004	4.589	0.004	0.713	-0.006
-0.297	-0.279	-0.552	0.004	-0.571	0.291	-0.343
0.014	0.433	-0.274	0.696	0.286	0.523	-0.017
0.295	0.014	-0.281	-0.006	-0.327	-0.017	0.462

Imaginary part.

0.055	-0.004	-0.128	-0.003	-0.204	0.013	0.359
0.001	0.041	0.060	0.242	-0.136	0.290	0.012
0.075	-0.026	-0.022	0.001	-0.167	-0.125	-0.182
0.002	-0.186	-0.001	0.000	0.001	0.186	-0.002
0.182	0.125	0.167	-0.001	0.022	0.026	-0.075
-0.012	-0.290	0.136	-0.242	-0.060	-0.041	-0.001
-0.359	-0.013	0.204	0.003	0.128	0.004	-0.055

Fig 19

The real and imaginary parts of the fourier transform of a unit cell shifted by (1.3,1.7). These shift values can be easily derived from the general formulas (7) and (8), or in particular (9) and (10) which are for specific lines. Using (9) we obtain:

$\alpha = 1.300$ (from the point (2,0))

$\beta = 1.704$ (from the point (0,2))

We could calculate various values of α and β to obtain an average if we desire. It should be noted that the number of values suitable for accurate determination of α and β is not very large. (In this case only about 9 different pairs.)

Real part.

-0.157	0.002	-0.031	-0.002	-0.173	0.013	0.380
-0.001	0.153	0.143	0.490	-0.248	0.478	0.019
-0.169	0.192	-0.459	0.004	-0.565	-0.306	-0.340
-0.005	0.670	0.004	4.589	0.004	0.670	-0.005
-0.340	-0.306	-0.565	0.004	-0.459	0.192	-0.169
0.019	0.478	-0.248	0.490	0.143	0.153	-0.001
0.380	0.013	-0.173	-0.002	-0.031	0.002	-0.157

Imaginary part.

0.439	-0.017	-0.350	-0.006	-0.302	0.014	0.270
-0.017	0.503	0.255	0.551	-0.180	0.209	0.004
-0.309	0.221	-0.340	0.002	-0.118	0.003	0.078
-0.004	0.309	0.001	0.000	-0.001	-0.309	0.004
-0.078	-0.003	0.118	-0.002	0.340	-0.221	0.309
-0.004	-0.209	0.180	-0.551	-0.255	-0.503	0.017
-0.270	-0.014	0.302	0.006	0.350	0.017	-0.439

Fig 20

The real and imaginary parts of the fourier transform of a unit cell shifted by (-2.2,4.3).

Derived shift values are:

$\alpha = -2.201$ (from the point (2,0))

$\beta = 4.298$ (from the point (0,2))

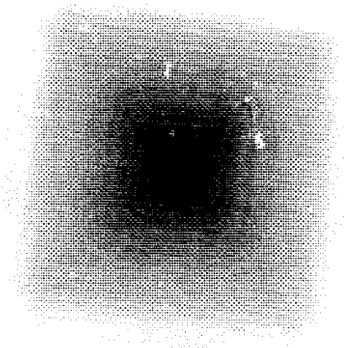

Fig 21
cf. Fig 3
Def = -800 Å
Th = 44 Å
Depth = 18.2
FWHM = 2.55 mrad

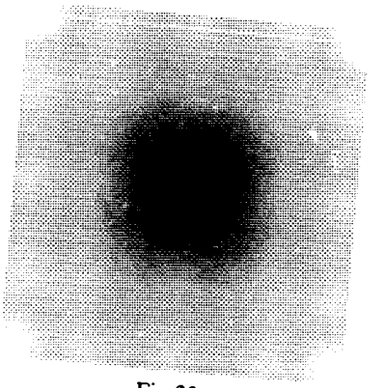

Fig 22
cf. Fig 6
Def = -800 Å
Th = 88 Å
Depth = 174.7
FWHM = 3.27 mrad

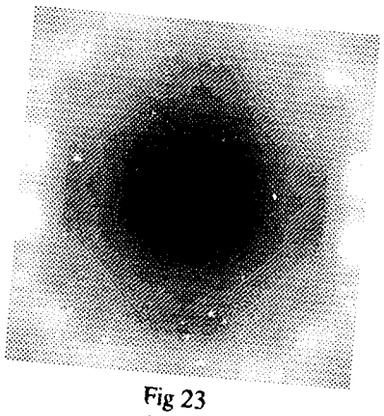

Fig 23
cf. Fig 9
Def = -800 Å
Th = 133 Å
Depth = 416.4
FWHM = 4.27 mrad

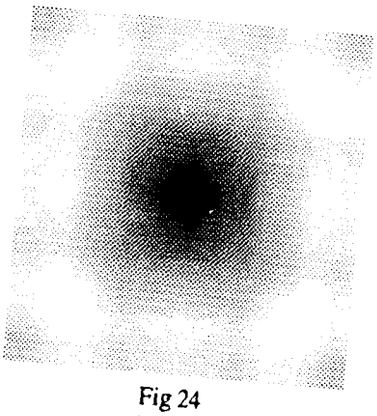

Fig 24
cf. Fig 10
Def = -1200 Å
Th = 133 Å
Depth = 263.4
FWHM = 2.73 mrad

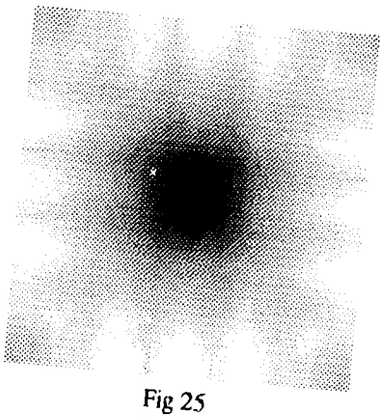

Fig 25
cf. Fig 13
Def = -1200 Å
Th = 177 Å
Depth = 414.4
FWHM = 2.34 mrad

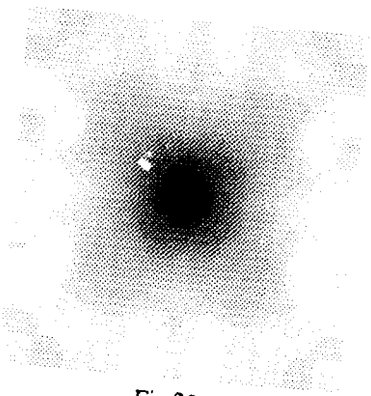

Fig 26
cf. Fig 15
Def = -800 Å
Th = 221 Å
Depth = 403.6
FWHM = 2.16 mrad

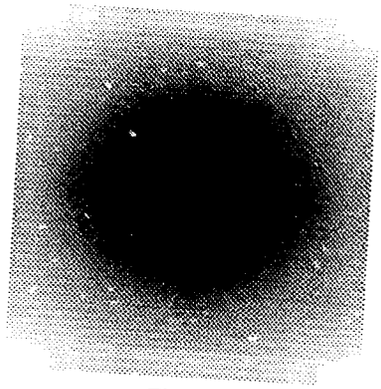

Fig 27
cf Fig 7
Def = -1200 Å
Th = 88 Å
8% edge

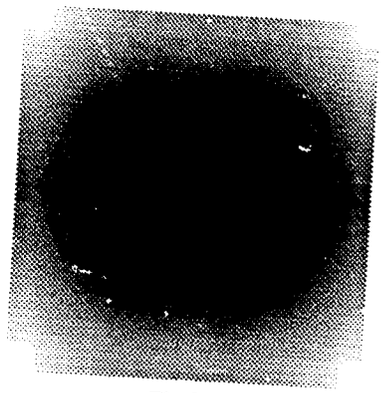

Fig 28
cf Fig 7
Def = -1200 Å
Th = 88 Å
22% edge

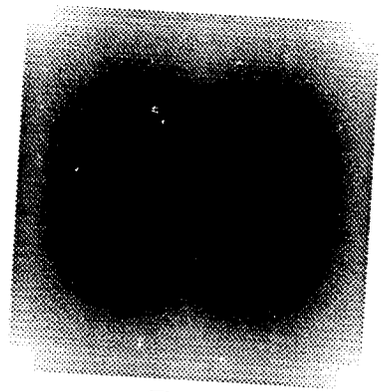

Fig 29
cf Fig 7
Def = -1200 Å
Th = 88 Å
39% edge

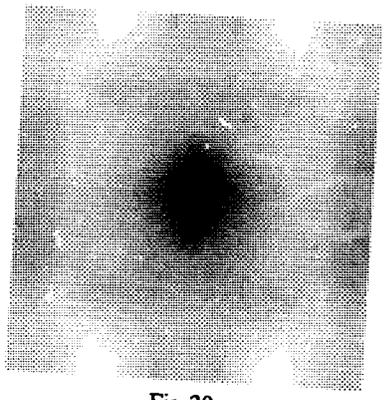

Fig 30
cf Fig 15
Def = -800 Å
Th = 221 Å
8% edge

Fig 31
cf Fig 15
Def = -800 Å
Th = 221 Å
22% edge

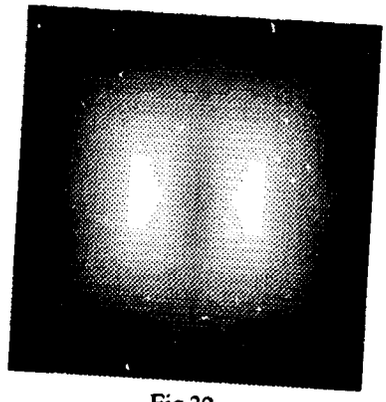

Fig 32
cf Fig 15
Def = -800 Å
Th = 221 Å
39% edge

Edge effects

Tilt maps produced as figs 7 and 15 except for the inclusion of some edge pixels. Edge pixels were placed to the right and top of the images since if placed all the way around they would not have changed the symmetry of the images, and we would therefore only be looking at the effect on the tilt maps of symmetric edges which would not be the case in practice.

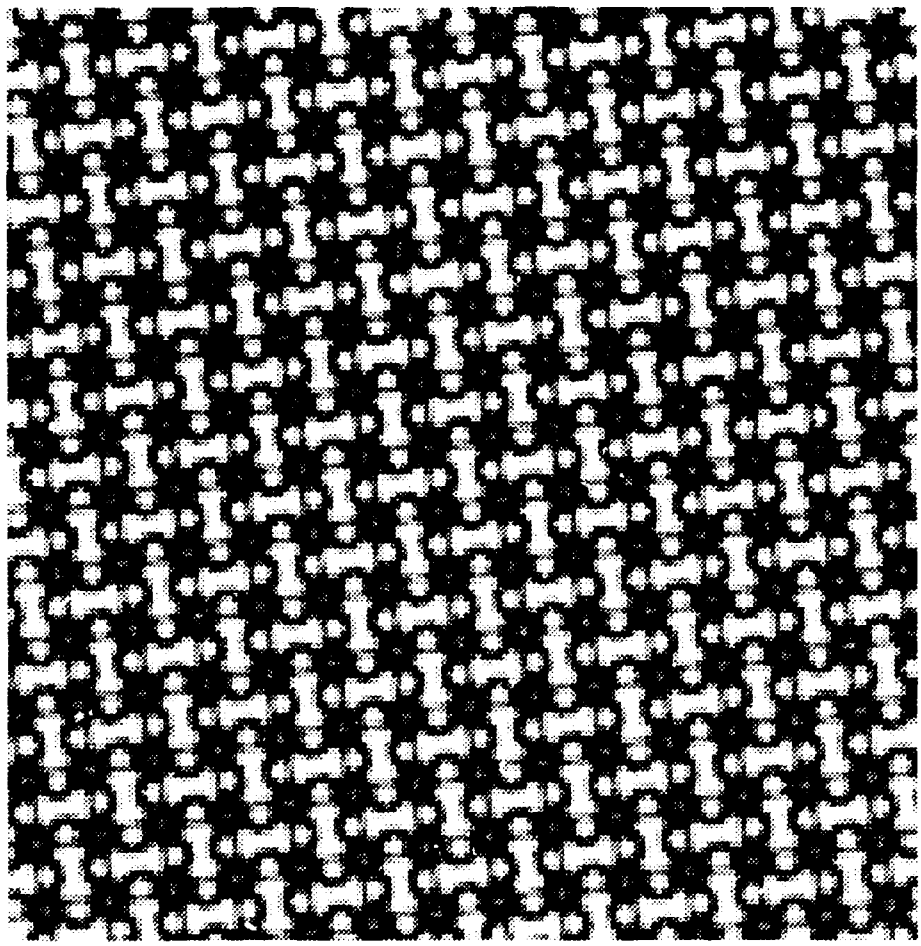

Fig 33

An array of unit cells that cannot be transformed into a square array using a simple linear transformation without losing some complete cells and therefore some potentially valuable information.

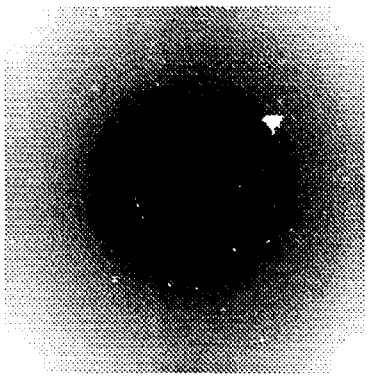

Fig 34
cf Fig 27
Def = -1200 Å
Th = 88 Å
Depth = 467.4 Å
8% edge blanked

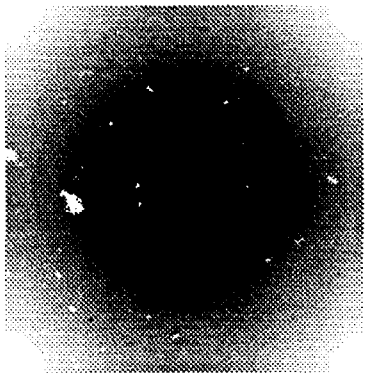

Fig 35
cf Fig 28
Def = -1200 Å
Th = 88 Å
Depth = 306.6 Å
22% edge blanked

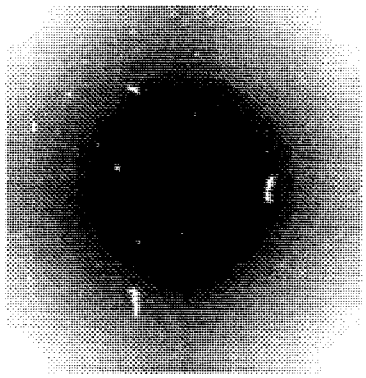

Fig 36
cf Fig 29
Def = -1200 Å
Th = 88 Å
Depth = 430.2 Å
39% edge blanked

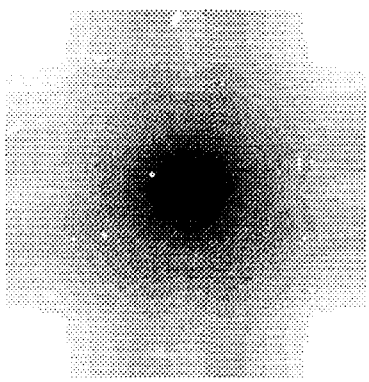

Fig 37
cf Fig 30
Def = -800 Å
Th = 221 Å
Depth = 714.52 Å
8% edge blanked

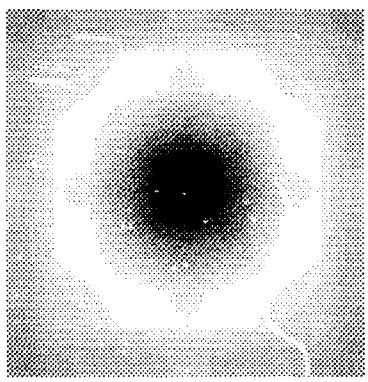

Fig 38
cf Fig 31
Def = -800 Å
Th = 221 Å
Depth = 334.7 Å
22% edge blanked

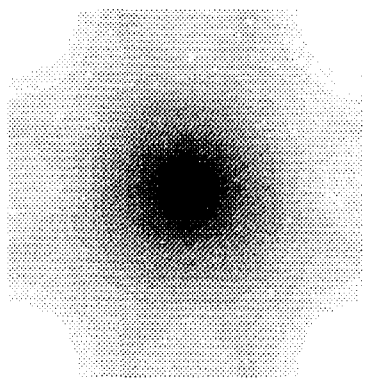

Fig 39
cf Fig 32
Def = -800 Å
Th = 221 Å
Depth = 629.2 Å
39% edge blanked

Reducing edge effects

Tilt maps resulting from edge pixels as introduced into the images to produce figs 27–32, set to zero.

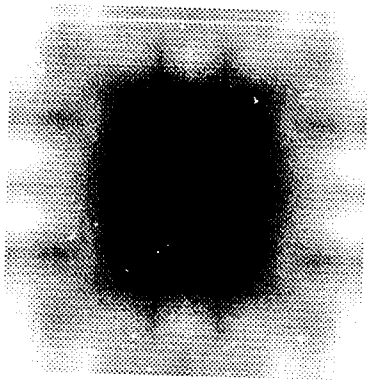

Fig 40a
cf. Fig 4
Def = -1200 Å
Th = 44 Å
Depth = 103.6

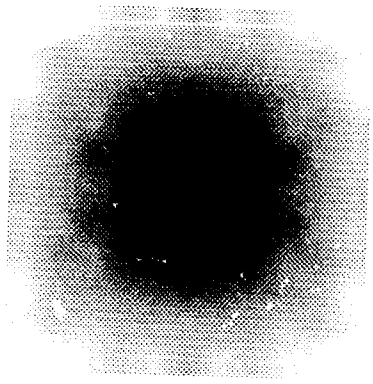

Fig 40b
cf. Fig 4
Def = -1200 Å
Th = 44 Å
Depth = 98.1

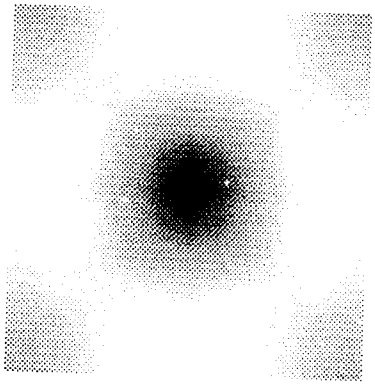

Fig 41a
cf. Fig 11
Def = -400 Å
Th = 177 Å
Depth = 569.6

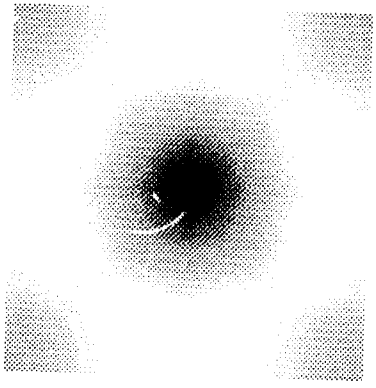

Fig 41b
cf. Fig 11
Def = -400 Å
Th = 177 Å
Depth = 513.2

Noise

Tilt maps produced from noisy images. Noise was added in SEMPER with a dose of 100. The tilt maps on the left had full averaging of the imaginary parts of the fourier transforms during analysis while those on the right had averaging only on the region shown in figure 17.

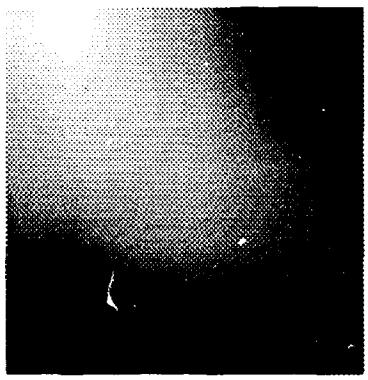

Fig 42

Def = -800 Å

Th = 177 Å

A quarter tilt map produced with the same images as used to obtain the full tilt map in figure 12, except that each of the images used here had a constant beam tilt of 7.36 mrad in the [010] direction. (Across the image as viewed here.) The aligned crystal orientation is displayed at the top left hand corner.